

Design of an untethered magbot: mimicking fruit fly larvae using magnetothermal actuation

Jianning Ding (✉ dingjn@ujs.edu.cn)

Jiangsu University

Lin Xu

Jiangsu University

Siyuan Liu

Jiangsu University

Robert Wagner

University of Colorado Boulder

Qingrui He

Jiangsu University

Xiang Zou

Jiangsu University

Yu Fu

Jiangsu University

Xingling Shi

Jiangsu University of Science and Technology

Dongliang Zhao

Southeast University

Franck Vernerey

University of Colorado Boulder

Research Article

Keywords: Soft robot, untethered, load-carrying, biomimetic, anisotropic friction

Posted Date: March 1st, 2022

DOI: <https://doi.org/10.21203/rs.3.rs-1347144/v1>

License: © ⓘ This work is licensed under a Creative Commons Attribution 4.0 International License.

[Read Full License](#)

Design of an untethered magbot: mimicking fruit fly larvae using magnetothermal actuation

Lin Xu^{1*}, Siyuan Liu^{1*}, Robert Wagner^{2*}, Qingrui He¹, Xiang Zou¹, Yu Fu¹, Xingling Shi³,
Jianning Ding^{1†}, Dongliang Zhao^{4†}, Franck Vernerey^{2†}

¹Institute of Intelligent Flexible Mechatronics, Jiangsu University, Zhenjiang 212013, P. R. China

²Department of Mechanical Engineering & Material Science and Engineering Program, University of Colorado at Boulder, Boulder 80309-0428, USA

³School of Materials Science and Engineering, Jiangsu University of Science and Technology, Zhenjiang 212003, P. R. China

⁴School of Energy and Environment, Southeast University, Nanjing 210096, P. R. China

*These authors contributed equally to this work.

†Corresponding author. Email: dingjn@ujs.edu.cn (J.D.); Email: dongliang_zhao@seu.edu.cn (D.Z.); franck.vernerey@colorado.edu (V.F.)

Key words: Soft robot, untethered, load-carrying, biomimetic, anisotropic friction.

Summary: We introduce a soft, biomimetic robot capable of untethered directional motion under external loads.

Abstract: Soft, worm-like robots show promise in complex and constrained environments due to their robust, yet simple movement patterns. Although many such robots have been developed, they either rely on tethered power supplies and complex designs or cannot move external loads. To address these issues, we here introduce a novel “magbot” that utilizes temperature-sensitive actuation and surface pattern-induced anisotropic friction to achieve peristaltic locomotion inspired by fly larvae. This simple, untethered design can carry cargo that weighs up to three times its own weight with only a 17% reduction in speed over unloaded conditions thereby demonstrating, for the first time, how soft, untethered robots may be used to carry loads in controlled environments. Given their small scale and low cost, we expect that these

27 magbots may be used in remote, confined spaces for small objects handling or as
28 components in more complex designs.

29 **INTRODUCTION**

30 The recent emergence of robots comprised of flexible materials rather than rigid
31 structures has introduced broad prospects in robotics engineering¹. Like soft creatures,
32 soft robots are highly deformables¹⁻³, thereby introducing several advantages over their
33 rigid counterparts. For example, soft robots may deform to the contours of confined
34 spaces and can exhibit continuous, multimodal deformations due to their flexibility,
35 making them highly sought after for traversal of complex environments⁴⁻⁹. Additionally,
36 soft materials are generally safer for human-machine interactions¹⁰ and exhibit higher
37 biocompatibility¹¹, rendering them suitable for both *in vivo* and *in vitro* applications¹².
38 Despite these advantages, there remain challenges pertaining to soft robots'
39 miniaturization, load carrying capacity, and autonomy. However, nature is rife with
40 living designs that have achieved all three features.

41 Soft invertebrates such as caterpillars^{13,14}, worms^{15,16}, and larvae of *Diptera* (i.e.,
42 flies)¹⁷ use peristaltic or wave-like actuation in conjunction with means of
43 asymmetrical anchoring to move reliably in their environments. These principals of soft
44 actuation and asymmetrical friction have recently inspired many designs for multi-
45 functional and highly adaptable soft, biomimetic robots¹⁸⁻²⁶. However, arguably the
46 simplest and most scalable designs utilize alternating bending and extension as their
47 only mode of actuation^{18,19}, thus negating the need for complex internal mechanisms,
48 control systems, or localized actuators as in the case of bots that replicate non-harmonic,
49 wave-like peristaltic actuation. Instead, these simple bots may be comprised entirely of
50 one or a few stimuli-sensitive materials³ thereby mitigating the need for hydro-
51 pneumatic umbilicals²⁰⁻²⁷ or electrical tethers²⁸⁻³¹ for their power supply. Furthermore,
52 while more complex systems achieve unidirectional motion using legs and adhesive
53 sites (mimicking caterpillars¹³) or localized lateral expansion and contraction
54 (replicating worms^{16,17}), simpler designs aspire to leverage anisotropic surface patterns

55 that cause asymmetric friction.^{18,19,32,33} These take inspiration from natural systems
56 such as hook-like formations occurring on the skin of fly larvae.¹⁷

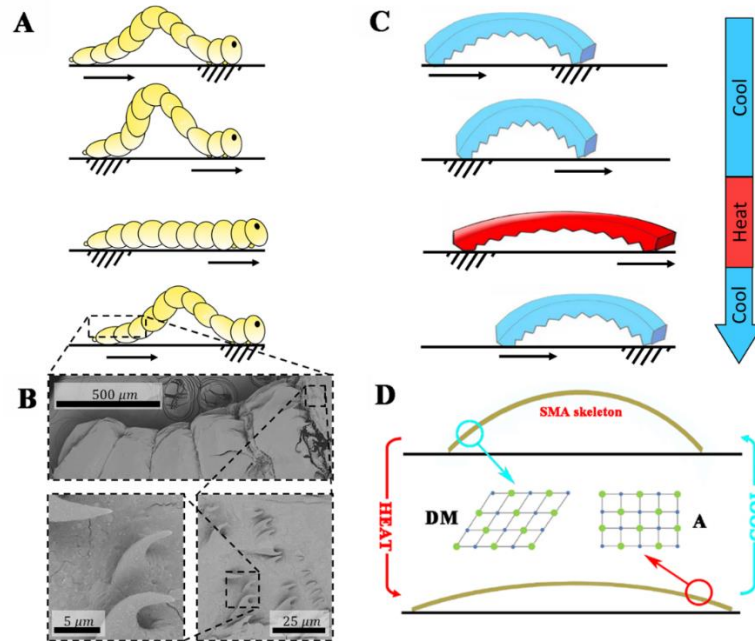
57 We here introduce a simple and scalable maggot-inspired robot or “magbot” that
58 utilizes unimodal bending and extension as its only means of actuation. It achieves
59 unidirectional motion via sawtooth-like geometries at its head and tail. The magbot’s
60 “skeleton” is comprised of shape-memory alloy (SMA)^{32,34–41} that actuates upon
61 heating. The SMA is heated using an alternating magnetic field from an induction coil.
62 While an external power supply is indispensable in this design, magnetic induction
63 eliminates the need for tethers and therefore physical restraints. In the remainder of this
64 work, we overview the design of the magbot, characterize its magnetothermal actuation,
65 and introduce the geometric feature that imposes asymmetric friction. We then
66 characterize the anisotropic friction, travel speed, and movement efficiency under
67 different external loads for magbots with three different pattern angles.

68 **RESULTS AND DISCUSSION**

69 **Design of the magbot.**

70 Fly lava movement is driven by cyclical phases in which the larva anchors its head,
71 pulls the trailing portions of its body forward, anchors its rear, and then pushes its head
72 forward (**Fig. 1A**). Anchoring is facilitated by microscopic, spine-like hooks along the
73 length of the larva’s body (see **Fig.1B** for SEM images). Directional motion ensues due
74 to anisotropic friction between the larvae and the substrate during anchoring. Based on
75 these observations, we fabricated bioinspired magbots according to the procedure
76 outlined in **Fig. S1** (see the **Materials and Methods** section for details). While
77 biological peristaltic motion generally involves multi-modal, wave-like propagation
78 along the length of a larva¹⁷, our simplified magbots simply have two contact regimes
79 – a head and tail – at any given moment. This permits the use of a simpler form of
80 harmonic, unimodal bending and extension. Actuation is achieved via a small SMA
81 skeletal strip embedded in the magbot. At low temperature, the SMA skeleton bends
82 (**Fig. 1C**) and is comprised of a detwinned martensite (DM) micro-structure (**Fig. 1D**).
83 At high temperature, the SMA structure changes from a DM phase to austenite (A)

84 phase (**Fig. 1D**), causing it to straighten. This process is reversible, such that periodic
 85 deformation of the skeleton can be remotely achieved using an alternating magnetic
 86 field that heats the SMA. Asymmetric anchoring is achieved through a wedge-shaped,
 87 anisotropic interface geometry inspired by the hook-like formations found on fly larvae
 88 (**Fig. 1B**).

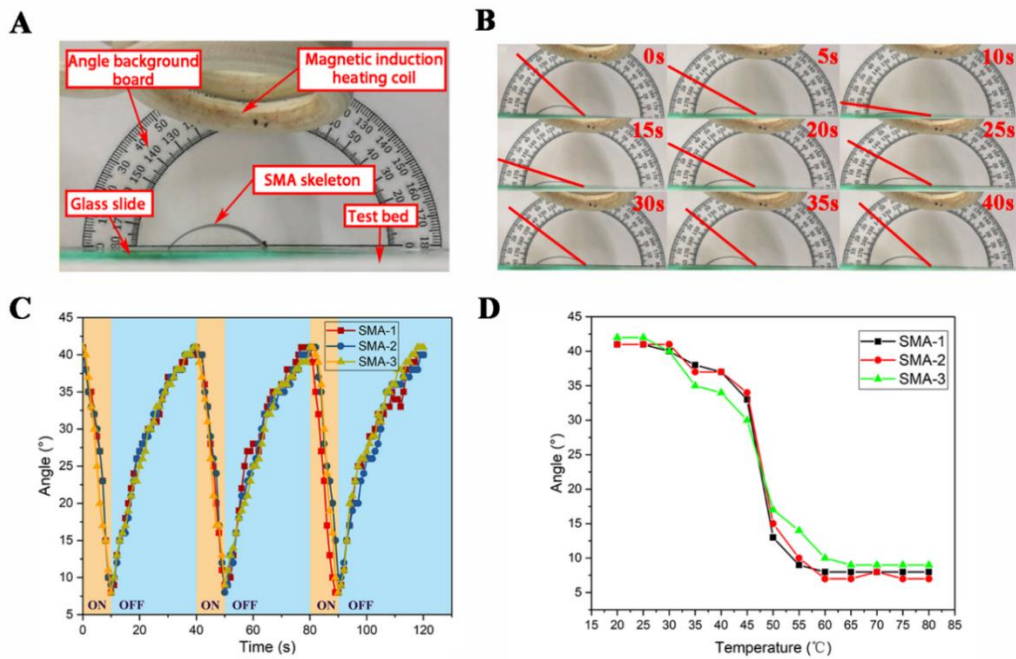


89
 90 **Fig 1. Schematic diagram of magbot.** (A) A schematic of fruit fly larva movement displays
 91 the phases of peristaltic motion in which a larva anchors its head, pulls its tail towards its head,
 92 anchors hind portions of its body, and then pushes its head forwards. In many organisms^{13,17}, such
 93 waves propagate non-harmonically along the creatures' lengths, however – for simplicity – this is
 94 not illustrated here. (B) Scanning electron microscopic images of the surface microstructure of fruit
 95 fly larvae display hook-like features that give rise to asymmetric friction. (C) A schematic of ideal,
 96 bio-inspired magbot motion is displayed under a cycle of heating and cooling. (D) A schematic of
 97 the SMA skeleton inside of a magbot illustrates the microstructural phase evolution within the alloy
 98 that drives magbot bending and extension as the microstructure alternates between detwinned
 99 martensite (DM) and austenite (A) phases. Movement in (A) and (C) is denoted by arrows while
 100 anchoring is denoted by crosshatching.

101 **Magneto-thermal deformation of the SMA skeleton.**

102 Magneto-thermal deformation of the SMA skeleton is characterized in **Fig.2**. **Fig.2A**
 103 displays the experimental setup used to quantify deformation. The sample resides on a
 104 glass plate, 40 mm above which the induction coil is positioned. To measure the
 105 deformation angle of the sample, a protractor is placed in the background so that its

106 center coincides with the right end of the sample, which is fixed in place. Deformation
 107 is quantified by the tangent angle to the SMA strip at the position of this fixed right side
 108 (**Fig. 2B**). A larger angle indicates a higher degree of bending (i.e., that the sample is
 109 closer to its reference state), while a lower angle indicates a higher degree of extension
 110 (i.e., that the sample is further from its reference state).
 111



112
 113 **Figure 2. Magneto-thermal deformation response of SMA actuator.** (A) The experimental setup
 114 used to measure magneto-thermal response of the SMA strip is shown. (B) One cycle of periodic
 115 deformation is displayed, with the tangent angle used to characterize deformation denoted by a red
 116 line. (C) Deformation angle is plotted with respect to time for three SMA skeletons undergoing three
 117 periods of reversible loading (each). (D) Deformation angle is plotted with respect to temperature
 118 of the SMA skeleton.

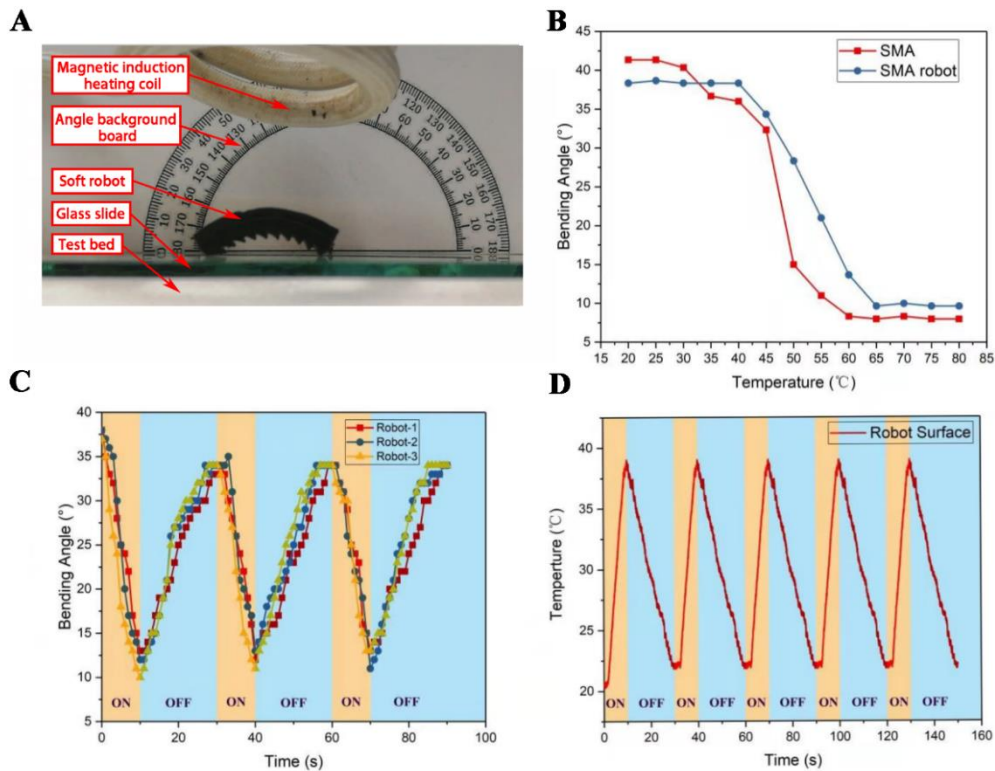
119 **Fig.2B** illustrates the measured bending angle at different times as the SMA
 120 sample undergoes heating due to magnetic induction. The corresponding response
 121 angles and SMA temperature are displayed in **Fig. 2C** and **Fig. 2D**, respectively. For
 122 each period of thermal loading, the magnetic field is introduced from 0-10 s and then
 123 removed from 10-40 s. Correspondingly, the bending angle of the sample starts at 41°,
 124 decreases to 8° (from 0→10 s) and then recovers to 37° (from 10→40 s). The bending
 125 angle repeatably completely recovers after 40 s (**Fig. 2 B-C**) and remains between 9-

126 41° throughout the entire cycle, exemplifying stability and reversibility. Note that
127 extensile actuation is slow in the early stages (41→30° in 0→5 s) and rapid in the later
128 stages (30→9° in 5→10 s) while bending recovery is rapid in the early stages (9→37°
129 from 10→30 s) and slow in the later stages. This effect is likely influenced by the rate
130 of heating and cooling, so to better understand actuation control with respect to
131 temperature, we examine **Fig. 2D**. This plot reveals a sharp phase transition from highly
132 bent (at low temperatures) to weakly bent (at high temperatures) at a temperature
133 around 45-50° C.

134 **Magnetothermal deformation of the magbot.**

135 The magnetothermal response of the magbot is characterized in **Fig. 3**. The
136 experimental setup (**Fig. 3A**) is identical to that used in **Fig. 2A**. Like the SMA sample,
137 the magbot exhibits good thermal deformation response with a bending angle ranging
138 from 10-38° (**Fig. 3B**), comparable to the un-skinned SMA skeleton (8~41°). However,
139 the thermal transition zone is more gradual and occurs between roughly 40~65° (as
140 opposed to 45-50° for the SMA alone), which is likely due to elastic resistance from the
141 soft skin. To ensure that this widened temperature range does not significantly impact
142 the latency of actuation, we examine the deformation and temperature responses with
143 respect to time (**Fig. 3C-D**).

144 **Fig.3C** shows the response of three distinct magbot prototypes, each with an initial
145 bending angle of 41°. For these experiments, magnetic heating occurs for 10 s, followed
146 by 20 s of cooling, and each sample is tested for three consecutive cycles. Notably the
147 presence of the elastic skin around the SMA sample restricts its deformation during
148 heating but also creates an elastic restoring force that accelerate its recovery to the
149 original state during cooling, hence the reduction in cooling time to 20 s. **Fig. 3C**
150 demonstrates that significant actuation is preserved over the timescale of 10¹ s, even
151 with the elastic skin. Furthermore, the deformation is nearly reversible from the first to
152 second cycle, and fully reversible thereafter.



153

154 **Figure 3. Magneto-thermal response behavior of SMA magbot.** (A) The experimental setup used
 155 to measure magneto-thermal response of the magbot is shown. (B) The average bending angle
 156 response of three magbot prototypes (blue circles) and three SMA skeletons (red squares) is plotted
 157 with respect to temperature. (C) Deformation angle is plotted with respect to time for three magbots
 158 undergoing three periods of reversible loading (each). (D) Average surface temperature of three
 159 magbots is plotted with respect to time for five periods of thermal loading.

160 **Fig.3D** presents the time evolution of the magbot's surface temperature during
 161 cyclic induction heating. We see that this temperature varies between 22-37 °C, which
 162 is lower than that of the SMA strip alone (40-65 °C). This is because induction heating
 163 acts on the SMA but not the external skin. Consequently, the internal temperature of the
 164 magbot (**Fig. 3B**) exceeds the external temperature measured by infrared thermal
 165 imagery (**Fig. 3D**). Therefore, the external skin not only reduces the timescale of
 166 bending recovery during cooling, but also reduces the surface temperatures of the
 167 magbots to a safer range for human handling or biological interfacing. A final and
 168 primary purpose of the external skin is to induce asymmetric surface interfaces and
 169 friction for locomotion.

170

171 **On the origins of asymmetric motion**

172 Unlike multimodal peristaltic motion^{13,17}, the first-harmonic actuation of the magbot is
173 symmetric and may not power directional motion without symmetry-breaking. Hence,
174 the asymmetric surface geometry along its bottom face, which consists of periodic,
175 “sawtooth”-like wedges whose angles may be adjusted (**Fig. 4**). While the geometry
176 was patterned for ease of mold design and fabrication, only the frontmost and rearmost
177 wedges remain in contact with the substrate throughout actuation and are therefore
178 significant. For convenience, we refer to these contact regions as the “forefoot” and
179 “hindfoot”, respectively.

180 To understand what causes asymmetric motion, we begin by considering the
181 external forces acting on the magbot during one actuation cycle (**Fig. 4A-B**). The only
182 external forces are body force due to gravity (F_w), the normal force from the substrate
183 at either foot (F_N), and the frictional forces acting on the forefoot (F^+) and hindfoot
184 (F^-). From **Fig. 4A-C**, only the frictional forces at the magbot’s feet act along the
185 direction of motion, so it is the difference between these forces during extension and
186 then bending that governs net displacement. We assume that the magbot’s weight is
187 evenly distributed between the feet such that the frictional forces may be written:

188
$$\begin{cases} F^+ = \mu^+ F_N \\ F^- = \mu^- F_N \end{cases} \quad (1)$$

189 where μ^+ and μ^- are the coefficients of friction for the forefoot and hindfoot,
190 respectively. Recognizing that the net displacement will scale with the unbalanced force
191 on the magbot, and inversely with its mass (m), we may write the following scaling
192 law:

193
$$\Delta x \sim \frac{1}{2}(\mu^+ - \mu^-)g, \quad (2)$$

194 where we have substituted the relationship $F_N = 0.5mg$ for the magnitude of normal
195 force, in which g is gravitational acceleration. This simple scaling intuitively suggests
196 that the gravitational constant and difference between the magbot’s fore and hindfoot
197 coefficients of friction ($\Delta\mu^\pm = \mu^+ - \mu^-$) influence the displacement of the system.
198 However, only $\Delta\mu$ dictates the sense of this motion.

199 As reported by (Tramsen, et al. 2017), many factors influence anisotropic friction

200 of deformable “sawtooth” surface structures as they slide over surfaces, including both
 201 substrate and sawtooth properties (e.g., surface roughness, stiffness, geometry, etc.).⁴²
 202 Furthermore, here the relative angle between the pattern’s tapered face and the
 203 horizontal substrate varies throughout actuation, likely effecting both μ^+ and μ^- .
 204 However, for the purposes of this work, we are merely concerned with the effects of
 205 pattern angle and treat μ^+ and μ^- as constants during extension and bending. However,
 206 both μ^+ and μ^- must still change between these two actuation phases for forwards
 207 motion to occur. As such, we instead adapt the terminology introduced by Tramsen, et
 208 al. (2017) and consider two relative motion types: Type I motion wherein the tapered
 209 face of the pattern leads, and the relative movement of the substrate is “along” the
 210 pattern (**Fig. 4C**) with a coefficient of friction μ_I ; and Type II motion in which the
 211 contact edge leads, and the relative movement of the substrate is “against” the pattern
 212 (**Fig. 4D**) with a coefficient of friction μ_{II} . As highlighted in **Fig. 4A-B**, the forefoot
 213 undergoes Type I relative motion during extension, and Type II during bending, while
 214 the hindfoot experiences the opposite. Thus, we may rewrite $\Delta\mu$ for extension and
 215 bending independently as:

$$216 \quad \begin{cases} \Delta\mu_{ext} = \mu_I - \mu_{II} \\ \Delta\mu_{bnd} = \mu_{II} - \mu_I \end{cases} \quad (3)$$

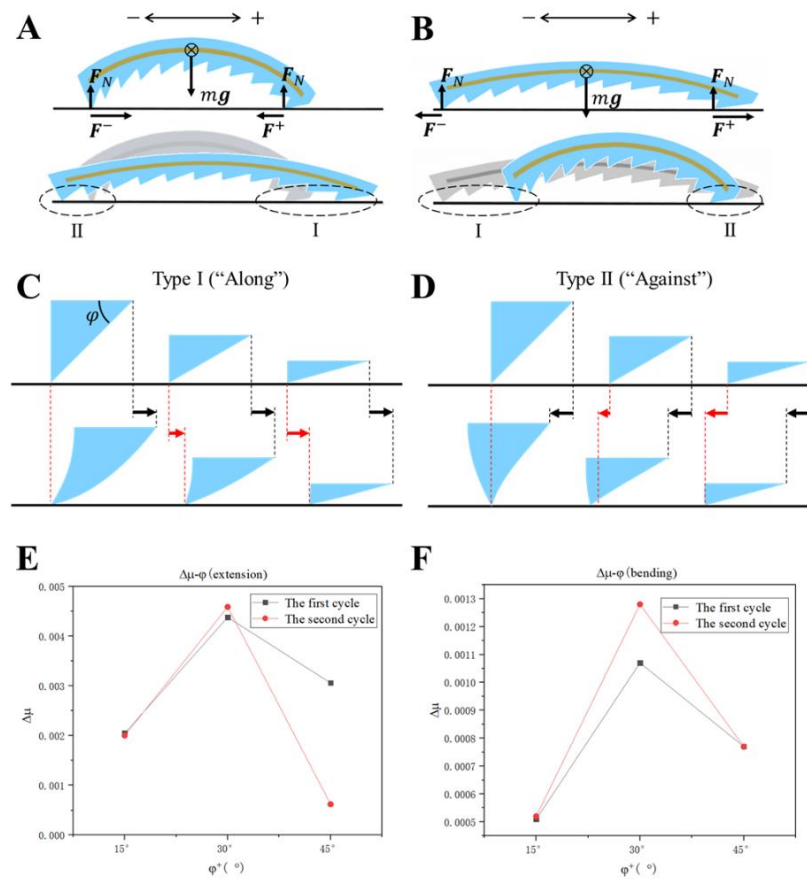
217 Let us now treat the frictional coefficients as always positive, so that we must explicitly
 218 indicate the directions of frictional forces through the signs of μ_I and μ_{II} (i.e., “ $-\mu$ ”
 219 implies that friction is driving the magbot backwards). Given this convention, we may
 220 rewrite **Eqn. 3** as:

$$221 \quad \begin{cases} \Delta\mu_{ext} = \mu_{II}^{ext} - \mu_I^{ext} \\ \Delta\mu_{bnd} = \mu_{II}^{bnd} - \mu_I^{bnd} \end{cases} \quad (4)$$

222 and so long as the frictional coefficient of movement against the pattern is greater than
 223 that along the pattern (i.e., $\mu_{II} > \mu_I$ or $\Delta\mu > 0$), forwards movement takes place.

224 The factors governing the magnitude of $\Delta\mu$ are not straightforward. In fact, as
 225 indicated by Tramsen, et al. (2017), even whether $\Delta\mu \geq 0$ is not guaranteed using a
 226 sawtooth pattern. However, for the system observed here, all values of $\Delta\mu$ are positive
 227 (**Fig. 4E-F**) (see the **Materials and Methods** section for estimation methods).

228 Interestingly, the order of magnitude of $\Delta\mu$ differs between bending and extension, with
 229 a much higher frictional difference during extension. This suggests that the majority in
 230 positional change occurs during extension. The factor likely driving this difference is
 231 the change in relative angle between the forefoot and hindfoot patterns with respect to
 232 the substrate. In effect, the coefficients of friction for Type I and Type II motion differ
 233 between the forefoot and hindfoot because the geometric conditions of these feet are
 234 not the same due to the magbot's bent conformation.



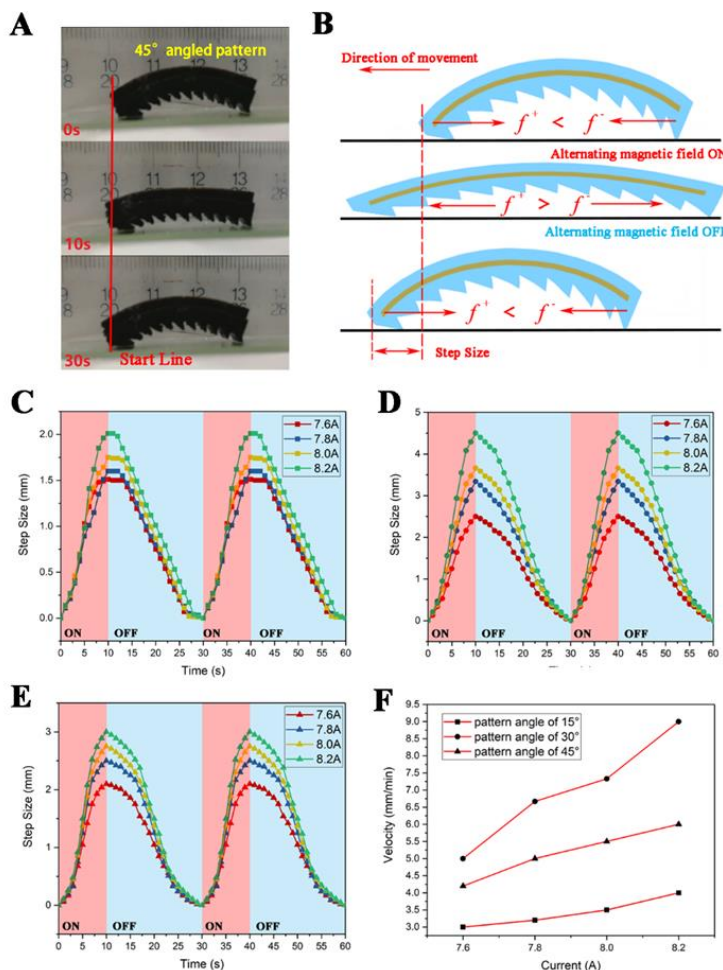
235
 236 **Figure 4. Analysis of asymmetric friction.** Free body diagrams and designations of Type I versus
 237 Type II motion are illustrated for the cases of (A) extension and (B) bending. (C) Type I motion
 238 “along” the sawtooth pattern and (D) Type II motion “against” the sawtooth pattern are illustrated.
 239 (C-D) Black arrows represent the relative actuation displacements of the SMA, while red arrows
 240 represent the realized displacement of the contact edges. Illustrations on the left represent the
 241 hypothesized extreme case for highly compliant members, in which none of the actuation
 242 displacement is realized as sliding during either actuation phase. In contrast, rightmost illustrations
 243 depict the case for rigid members, in which nearly all the actuation displacement is realized as
 244 sliding. A more optimal case in which more actuation displacement is realized during Type I motion
 245 than Type II motion, is illustrated in the center. (E-F) The experimentally estimated relationship
 246 between $\Delta\mu$ and ϕ during (E) extension and (F) bending is depicted for two cycles, highlighting its
 247 biphasic nature.

248 Significantly, during both actuation stages, $\Delta\mu$ shows a biphasic relationship with
249 respect to φ with the biggest values occurring for the intermediate pattern angle of $\varphi =$
250 30° (**Fig. 4E-F**). While to fully understand the origins of this optimization would
251 require an in-depth mechanical analysis, we here propose one possible explanation.
252 Tramsen, et al. (2017) recognized that the compliance of the sawtooth member greatly
253 impacts the effective frictional coefficient of the system. We posit that differences in
254 the “effective” coefficients of friction observed here must occur due to this compliance-
255 dependent, macroscale deformation since the microscale properties of the magbot skin
256 and substrate (e.g., surface roughness⁴³) remain constant. Specifically, we assert that
257 more compliant designs, here occurring for higher pattern angles, may undergo larger
258 strains before enough load is transmitted to break static friction and sliding ensues. In
259 the extreme case, it is possible that during both extension and bending, none of the
260 actuation displacement is realized as foot motion (see **Fig. 4E-F**, leftmost depictions).
261 Under such circumstances, no relative movement of the magbot would occur. Similarly,
262 for highly rigid designs (achieved through smaller pattern angles), enough load may be
263 transmitted from the SMA-skin interface to rapidly break static friction at the contact
264 edge, such that both feet slide nearly instantaneously during either actuation stage (see
265 **Fig. 4E-F**, rightmost depictions). Under these circumstances, both feet would slide
266 symmetrically about the center of mass of the magbot and no forwards motion would
267 occur. Therefore, there appears to exist an optimal angle that maximizes $\Delta\mu$ during both
268 stages of actuation. In future work, to optimize travel speed for specific applications,
269 we may quantitatively characterize the deformations undergone prior to breaking static
270 friction for each foot, using a combination of nonlinear, hyperplastic finite element
271 analysis and experimentation.

272 **Quantifying magbot motion.**

273 We here quantify magbots’ movements and speeds as they undergo multiple actuation-
274 recovery cycles on a level, rigid, glass substrate. **Fig. 5A** depicts a magbot with $\varphi =$
275 45° as it undergoes a single loading cycle and moves leftwards. For additional
276 visualization, see **Movies S1-S3**. Starting from a bent state (0 s), the alternating

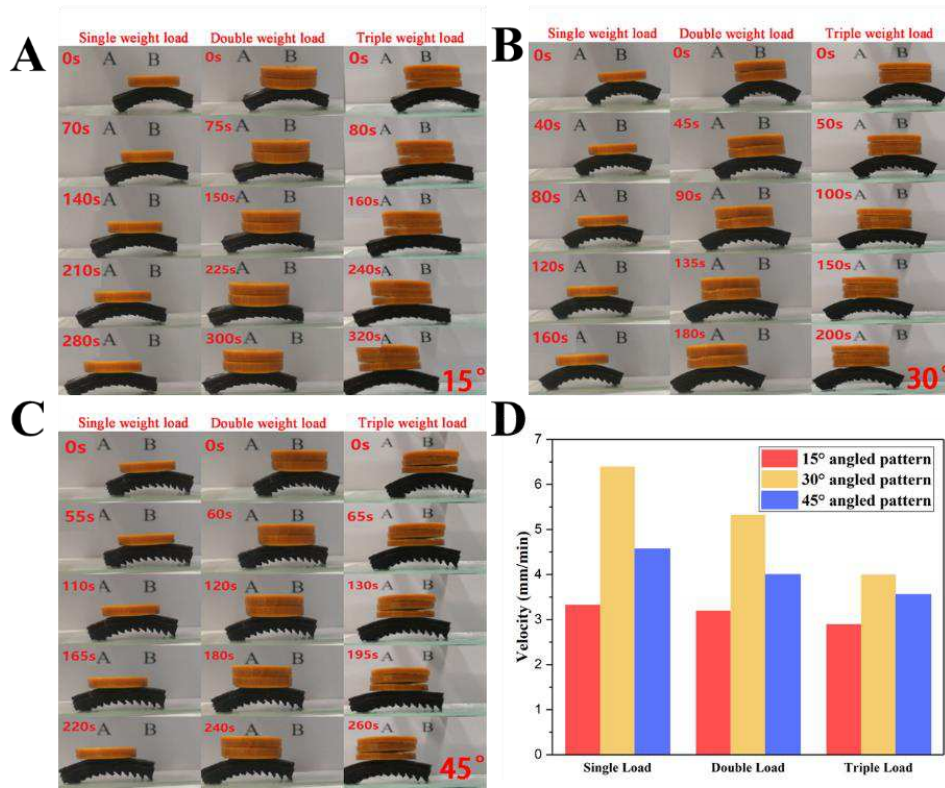
277 magnetic field is turned on to induce extension of the magbot (10 s). Ceasing magnetic
 278 actuation at 10 s, the magbot cools and bends back to its original state, marking the
 279 beginning of the next cycle.



280
 281 **Figure 5. Motion principle and kinematic behavior analysis of magbot.** (A) Snapshots of a
 282 magbot undergoing one thermal load cycle display movement leftwards. The top snapshot is
 283 presented at the beginning of heating (0 s); the middle snapshot is shown at the end of heating and
 284 beginning of cooling (10 s); and the bottom snapshot depicts the end of cooling (30 s). (B) A
 285 schematic illustrates the direction of frictional forces on the forefoot (f^+) and hindfoot (f^-) as well
 286 as the emergent step size after one loading cycle (not to scale). (C-E) Step sizes are plotted with
 287 respect to time for magbots with (C) 15°, (D) 30°, and (E) 45° pattern angles for two cycles of
 288 thermal loading, over a range of magnetically induced currents ($I \in [7.6, 8.2]$ A). (F) Velocity is
 289 plotted with respect to induction current for magbots with pattern angles of 15° (squares), 30°
 290 (circles), and 45° (triangles).

291 As expected, the asymmetric patterns induce directional motion (Fig. 5B). During the
 292 extension phase, the forefoot friction is oriented backwards (i.e., opposes net forward

293 movement), and the hindfoot friction is forwards (i.e., encourages net forward
 294 movement). However, the forefoot's friction coefficient is smaller than that of the
 295 hindfoot during extension, as evidenced by a finite translation Δ_e of the of the magbot
 296 leftwards. By contrast, during the recovery phase, the forefoot's friction is forwards,
 297 while the hindfoot's friction is backwards. Yet, as during heating, the difference in
 298 frictional coefficients during cooling induces a forward translation with step size Δ_r .
 299 Together, a full cycle yields a combined step size of $\Delta = \Delta_e + \Delta_r$ and the velocity of a
 300 magbot is defined as $v = \Delta/T$ where T is the full cycle time.



301
 302 **Figure 6. Load motion experiment of magbot with different angled pattern.** (A-C) Magbots
 303 with (A) 15°, (B) 30°, and (C) 45° are displayed, each undergoing one cycle of loading
 304 (chronologically from **top-to-bottom**) while carrying loads that are (left) 1×, (center) 2×, and
 305 (right) 3× their body weight.. (D) Travel speeds of magbots with different pattern angles of (red)
 306 15°, (yellow) 30°, and (blue) 45° under loads of (left) 1×, (center) 2×, and (right) 3× a magbot's
 307 body weight are displayed.

308 **Fig.5C, D and E** show experimental results of the maximum step size of a magbot
 309 for various pattern angles (15°, 30° and 45°, respectively) over a range of different
 310 induction currents (correlating directly to the magnetic field strength). The

311 corresponding velocities for all three pattern angles are plotted with respect to the
312 induction current (proportional to magnetic field strength) in **Fig. 5F**. While we observe
313 a monotonic increase in step size with respect to magnetic field strength (**Fig. 5F**), we
314 see a biphasic relationship between step size and pattern angle. Specifically, the
315 maximum step sizes, and therefore highest movement speeds, at any given induction
316 current are achieved by the magbot with the intermediate pattern angle of 30° (see **Fig.**
317 **5C-E or F**), for reasons as postulated in the previous section. In contrast, the magbot
318 with the pattern angle of 15° displays the minimum step size and slowest movement
319 speed.

320 **Cargo carrying by an unbound, soft magbot.**

321 In addition to characterizing the movement of unburdened magbots, we also assess their
322 efficiency while carrying external loads. For this, we carried out experiments in which
323 cargo was placed centrally on top of the magbots (**Fig. 6A-C**, and **Movies S5-S12**).
324 Cargo loads of $1\times$, $2\times$ and $3\times$ a magbot's body weight were studied. Motion efficiency
325 under these three loads for the three pattern angles (15° , 30° and 45°), are reported in
326 **Fig. 6D**. The induction current was maintained at 8.2 A. Generally, these results show
327 that the speed of a magbot is only moderately affected by cargo whose weight is on the
328 order of the magbot's body weight. The trend in speed reduction is consistent across all
329 three pattern angles and the intermediate angle (30°) still yields the fastest motion in all
330 cases. The loss in speed remains less than 50%, even when the cargo load is three times
331 the magbot's body weight. This indicates that, at least for magbots fabricated at this
332 length scale, their specific weight-carrying capacity renders them eligible for cargo
333 transport applications.

334 **CONCLUSIONS**

335 This study leverages the first principles of soft actuation and anisotropic
336 geometries regularly coupled in nature to induced peristaltic motion. While organisms
337 such as fly larvae utilize multimodal deformations and microscopic surface patterns to
338 induce ordered locomotion¹⁷, we here distilled these mechanisms into simple analogues
339 of harmonic, unimodal (bending) actuation and a macroscopic wedge-shaped interface

340 geometry. This allowed for the fabrication of maggot-inspired robots that locomote
341 unidirectionally. Their actuation is achieved via a magneto-thermo-responsive SMA
342 skeleton, while the anisotropic geometry is introduced by a soft enveloping skin that
343 serves the secondary purposes of thermal insulation. The simplicity of this design is
344 advantageous in a few ways. Firstly, to our knowledge this magbot is the first such soft
345 robot that displays targeted motion while carrying load without a tethered power supply.
346 Secondly, the lack of complex mechanisms in this design renders it inherently scalable.
347 The magbots' minimalist compositions could be feasibly fabricated at smaller length
348 scales using scalable molding methods or 3D printing. Additionally, the frictional
349 model introduced here is not inertial, implying that the mechanisms driving movement
350 would still apply at smaller scales in dry environments. Finally, these magbots display
351 relatively high specific-weight carrying capacities that would likely improve as their
352 length scale is decreased, as governed by square-cube scaling laws.

353 Nevertheless, these magbots are not without limitations. Most notably, the
354 timescale of actuation is on the order of 10^1 s, while the length scale of travel is on the
355 order of 10^{-3} m such that the normalized travel speeds are on the order 10^{-2} body lengths
356 per minute. Furthermore, the current study only examines the movement of these
357 magbots on level substrates, and early proof-of-concept work in their motility up
358 inclines indicates a further reduction in movement speed. As such, future work will
359 focus on improving the travel speed of magbots in the absence of load. In any case, the
360 advantages of flexibility, untethered motion, scalability, and high specific load-carrying
361 capacity exemplified in this work render this magbot and the minimalist design
362 philosophy employed here promising for applications in which soft-body transport must
363 occur through small spaces, over long distances, or with cargo in tow. Prospective
364 applications include monitoring of pipelines for damage detection, geological
365 exploration, or remote small object recovery from confined spaces.

366 **MATERIALS AND METHODS**

367 **Fabrication of the magbots.**

368 The fabrication process of the magbot is shown in **Fig.S1**. A rectangular specimen (20

369 mm × 4 mm × 0.1 mm) of shape memory alloy was fabricated using laser cutting
370 (Eagle, X-6060). An A-type silica gel (EcoFlex 00-30, Smooth-on) and B silica gel were
371 mixed with a 1:1 mass ratio. Mixing was conducted using a magnetic stirrer for 10
372 minutes. The mixture was then poured into rectangular molds housing the SMA
373 skeletons and containing pattern angles of 15°, 30° and 45°. The molds were allowed
374 to sit for 20 minutes to ensure that bubbles in the material completely escaped. They
375 were then placed in a vacuum drying box at 80° C for 4 hours. Once the molds were
376 removed, they were cooled to room temperature. The magbots with pattern angles of
377 15°, 30° and 45° had masses of 0.6040 g, 0.6000 g, and 0.6845 g, respectively. All
378 magbots' dimensions were approximately 42 mm × 6 mm × 4 mm.

379 **Control of magnetothermal deformation.**

380 The cyclic actuation of the SMA skeletons and fully fabricated magbots were assessed
381 using the experimental set ups depicted in **Fig. 2A** and **Fig. 3A**, respectively.
382 Temperature was increased from 20→80 °C in increments of 5 °C and the equilibrium
383 bending angle, was recorded at each temperature. Surface temperature readings were
384 measured by an infrared imaging system, FLIR T540. Actuation time (10 s) was taken
385 as the time needed for the samples to reach their bent, equilibrium states upon heating.
386 Similarly, restoration times (30 s for the SMA and 20 s for the magbot) were taken as
387 the times needed for the specimens to recover to their initial shapes via ambient cooling.
388 To obtain statistically relevant measurements, these tests were performed on three
389 different samples and each sample was tested three times. To report the time-
390 dependence of actuation and temperature, measurements were taken with a frequency
391 of 1 Hz.

392 **Testing the magbots.**

393 The magbots were placed onto level glass substrates and exposed to the 30 s thermal
394 cycles described above. Travel speeds were recorded as the step size (see **Fig. 5B**) per
395 unit time over multiple actuation cycles. Speeds were measured under various induction
396 currents (ranging from 7.6 A, 7.8 A, 8.0 A, and 8.2 A at alternating frequencies of 425

397 kHz) and pattern angles (of 15°, 30°, and 45°). The speeds of the magbots were
 398 measured both without (**Fig. S2, Movies S1-S3**) and with (**Movies S4-S12**) cargo loads
 399 as depicted in **Fig. 5A** and **Fig. 6A-C**, respectively. An induction current of 8.2 A was
 400 used for the loaded conditions. The masses used (0.6138 g, 0.6129 g, and 0.6151 g)
 401 were each on the order of one magbot body weight and were placed on top of the
 402 magbots' centers. The method of graphical speed measurement is illustrated through
 403 **Fig. S2**. The full set of measured travel speeds and efficiencies (with respect to
 404 unloaded speed) for magbots carrying 0×, 1×, 2×, and 3× their own BW are reported
 405 in **Table 1**. Parameters were conserved throughout experiments, unless specified
 406 otherwise (e.g., as in the cases of pattern angle, induction current, and cargo weight).

407 **Table 1** Speed of magbots under various loading conditions using an induction current of 8.2A.

Cargo Load (×BW)	Speed (mm/min) (% Efficiency = % Unloaded Speed/Loaded Speed)		
	15° angled pattern	30° angled pattern	45° angled pattern
0×	4.00 (100%)	9.00 (100%)	6.00 (100%)
1×	3.33 (83%)	6.40 (71%)	4.57 (76%)
2×	3.20 (80%)	5.33 (59%)	4.00 (67%)
3×	2.90 (73%)	4.57 (51%)	3.56 (59%)

408 **Characterizing anisotropic friction.**

409 To estimate the friction parameter, $\Delta\mu$, the geometric centers of the magbots were
 410 tracked across discrete frames of video footage. Their average accelerations along the
 411 horizontal axis during bending and extension were approximated using finite
 412 differences in position (Δx) and time (Δt) between frames as $\bar{a} \approx \Delta x / \Delta t^2$. Considering
 413 the forces acting on the magbot (**Fig. 4A-B**), the net unbalanced force along the
 414 horizontal axis can be written as:

415
$$m \frac{\Delta x}{\Delta t^2} \approx ma = \frac{mg}{2} (\mu^+ - \mu^-), \quad (5)$$

416 from which the anisotropic friction coefficient may be isolated as:

417
$$\Delta\mu \approx \frac{2\Delta x}{g\Delta t^2}. \quad (6)$$

418 **Eqn. 6** was used to estimate the values reported in **Fig. 4E-F**.

419 **REFERENCES AND NOTES**

- 420 1. Ilami M, Bagheri H, Ahmed R, Skowronek EO, Marvi H. Materials, Actuators, and Sensors for
421 Soft Bioinspired Robots. *Advanced Materials*. 2021;33(19):2003139.
- 422 2. Joseph VS, Calais T, Stalin T, Jain S, Thanigaivel NK, Sanandiya ND, Valdivia y Alvarado P.
423 Silicone/Epoxy Hybrid Resins with Tunable Mechanical and Interfacial Properties for Additive
424 Manufacture of Soft Robots. *Applied Materials Today*. 2021;22100979.
- 425 3. Cunha MP da, Debije MG, Schenning APHJ. Bioinspired Light-Driven Soft Robots Based on
426 Liquid Crystal Polymers. *Chem. Soc. Rev.* 2020;49(18):6568–6578.
- 427 4. Sun J, King JP, Pollard NS. Characterizing Continuous Manipulation Families for Dexterous Soft
428 Robot Hands. *Frontiers in Robotics and AI*. 2021;870.
- 429 5. Ju Y, Hu R, Xie Y, Yao J, Li X, Lv Y, Han X, Cao Q, Li L. Reconfigurable Magnetic Soft Robots
430 with Multimodal Locomotion. *Nano Energy*. 2021;87106169.
- 431 6. Zhou D, Zuo W, Tang X, Deng J, Liu Y. A Multi-Motion Bionic Soft Hexapod Robot Driven by
432 Self-Sensing Controlled Twisted Artificial Muscles. *Bioinspir. Biomim.* 2021;16(4):045003.
- 433 7. Joyee EB, Szmelter A, Eddington D, Pan Y. 3D Printed Biomimetic Soft Robot with Multimodal
434 Locomotion and Multifunctionality. *Soft Robotics*. 2020.
- 435 8. Monje Micharet CA, Laschi C. Editorial: Advances in Modeling and Control of Soft Robots.
436 *Frontiers in Robotics and AI*. 2021;8147.
- 437 9. Shah DS, Powers JP, Tilton LG, Kriegman S, Bongard J, Kramer-Bottiglio R. A Soft Robot That
438 Adapts to Environments through Shape Change. *Nat Mach Intell*. 2021;3(1):51–59.
- 439 10. Xu F, Wang H. Soft Robotics: Morphology and Morphology-Inspired Motion Strategy. *IEEE/CAA*
440 *Journal of Automatica Sinica*. 2021;8(9):1500–1522.
- 441 11. Guix M, Mestre R, Patiño T, De Corato M, Fuentes J, Zarpellon G, Sánchez S. Biohybrid Soft
442 Robots with Self-Stimulating Skeletons. *Science Robotics*. 2021;6(53):eabe7577.
- 443 12. Cianchetti M, Ranzani T, Gerboni G, Nanayakkara T, Althoefer K, Dasgupta P, Menciassi A. Soft
444 Robotics Technologies to Address Shortcomings in Today’s Minimally Invasive Surgery: The
445 STIFF-FLOP Approach. *Soft Robotics*. 2014;1(2):122–131.
- 446 13. Simon MA, Woods WA, Serebrenik YV, Simon SM, van Griethuijsen LI, Socha JJ, Lee W-K,
447 Trimmer BA. Visceral-Locomotory Pistoning in Crawling Caterpillars. *Current Biology*.
448 2010;20(16):1458–1463.
- 449 14. Plaut RH. Mathematical Model of Inchworm Locomotion. *International Journal of Non-Linear*
450 *Mechanics*. 2015;7656–63.
- 451 15. Zhan X, Fang H, Xu J, Wang K-W. Planar Locomotion of Earthworm-like Metameric Robots. *The*
452 *International Journal of Robotics Research*. 2019;38(14):1751–1774.
- 453 16. Quillin KJ. Kinematic Scaling of Locomotion by Hydrostatic Animals: Ontogeny of Peristaltic
454 Crawling by the Earthworm *Lumbricus Terrestris*. *Journal of Experimental Biology*.
455 1999;202(6):661–674.
- 456 17. Berrigan D, Pepin DJ. How Maggots Move: Allometry and Kinematics of Crawling in Larval
457 Diptera. *Journal of Insect Physiology*. 1995;41(4):329–337.
- 458 18. Vernerey F, Shen T. The Mechanics of Hydrogel Crawlers in Confined Environment. *Journal of*
459 *The Royal Society Interface*. 2017;14(132):20170242.
- 460 19. Shen T, Font MG, Jung S, Gabriel ML, Stoykovich MP, Vernerey FJ. Remotely Triggered
461 Locomotion of Hydrogel Mag-Bots in Confined Spaces. *Scientific Reports*. 2017;7(1):16178.

- 462 20. Morin SA, Shepherd RF, Kwok SW, Stokes AA, Nemiroski A, Whitesides GM. Camouflage and
463 Display for Soft Machines. *Science*. 2012;337(6096):828–832.
- 464 21. Wehner M, Truby RL, Fitzgerald DJ, Mosadegh B, Whitesides GM, Lewis JA, Wood RJ. An
465 Integrated Design and Fabrication Strategy for Entirely Soft, Autonomous Robots. *Nature*.
466 2016;536(7617):451–455.
- 467 22. Galloway KC, Becker KP, Phillips B, Kirby J, Licht S, Tchernov D, Wood RJ, Gruber DF. Soft
468 Robotic Grippers for Biological Sampling on Deep Reefs. *Soft Robotics*. 2016;3(1):23–33.
- 469 23. Yuk H, Lin S, Ma C, Takaffoli M, Fang NX, Zhao X. Hydraulic Hydrogel Actuators and Robots
470 Optically and Sonically Camouflaged in Water. *Nat Commun*. 2017;8(1):14230.
- 471 24. Martinez RV, Branch JL, Fish CR, Jin L, Shepherd RF, Nunes RMD, Suo Z, Whitesides GM.
472 Robotic Tentacles with Three-Dimensional Mobility Based on Flexible Elastomers. *Advanced*
473 *Materials*. 2013;25(2):205–212.
- 474 25. Hawkes EW, Blumenschein LH, Greer JD, Okamura AM. A Soft Robot That Navigates Its
475 Environment through Growth. *Science Robotics*. 2017;2(8):eaan3028.
- 476 26. Ishida M, Drotman D, Shih B, Hermes M, Luhar M, Tolley MT. Morphing Structure for Changing
477 Hydrodynamic Characteristics of a Soft Underwater Walking Robot. *IEEE Robotics and*
478 *Automation Letters*. 2019;4(4):4163–4169.
- 479 27. Li S, Stampfli JJ, Xu HJ, Malkin E, Diaz EV, Rus D, Wood RJ. A Vacuum-Driven Origami “Magic-
480 Ball” Soft Gripper. In *2019 International Conference on Robotics and Automation (ICRA)*; 2019;
481 pp. 7401–7408.
- 482 28. Shintake J, Rosset S, Schubert B, Floreano D, Shea H. Versatile Soft Grippers with Intrinsic
483 Electroadhesion Based on Multifunctional Polymer Actuators. *Advanced Materials*.
484 2016;28(2):231–238.
- 485 29. Kofod G, Wirges W, Paajanen M, Bauer S. Energy Minimization for Self-Organized Structure
486 Formation and Actuation. *Appl. Phys. Lett*. 2007;90(8):081916.
- 487 30. Pei Q, Rosenthal M, Stanford S, Prahlah H, Pelrine R. Multiple-Degrees-of-Freedom
488 Electroelastomer Roll Actuators. *Smart Mater. Struct*. 2004;13(5):N86–N92.
- 489 31. Jung K, Koo JC, Nam J, Lee YK, Choi HR. Artificial Annelid Robot Driven by Soft Actuators.
490 *Bioinspir. Biomim*. 2007;2(2):S42–S49.
- 491 32. Sheng X, Xu H, Zhang N, Ding N, Zhu X, Gu G. Multi-Material 3D Printing of Caterpillar-
492 Inspired Soft Crawling Robots with the Pneumatically Bellow-Type Body and Anisotropic Friction
493 Feet. *Sensors and Actuators A: Physical*. 2020;316112398.
- 494 33. Wang X, Yang B, Tan D, Li Q, Song B, Wu Z-S, del Campo A, Kappl M, Wang Z, Gorb SN, *et al*.
495 Bioinspired Footed Soft Robot with Unidirectional All-Terrain Mobility. *Materials Today*.
496 2020;3542–49.
- 497 34. Mao S, Dong E, Jin H, Xu M, Zhang S, Yang J, Low KH. Gait Study and Pattern Generation of a
498 Starfish-like Soft Robot with Flexible Rays Actuated by SMAs. *J Bionic Eng*. 2014;11(3):400–
499 411.
- 500 35. Wang W, Lee J-Y, Rodrigue H, Song S-H, Chu W-S, Ahn S-H. Locomotion of Inchworm-Inspired
501 Robot Made of Smart Soft Composite (SSC). *Bioinspir. Biomim*. 2014;9(4):046006.
- 502 36. Song S-H, Kim M-S, Rodrigue H, Lee J-Y, Shim J-E, Kim M-C, Chu W-S, Ahn S-H. Turtle
503 Mimetic Soft Robot with Two Swimming Gaits. *Bioinspir. Biomim*. 2016;11(3):036010.
- 504 37. Villanueva A, Smith C, Priya S. A Biomimetic Robotic Jellyfish (Robojelly) Actuated by Shape
505 Memory Alloy Composite Actuators. *Bioinspir. Biomim*. 2011;6(3):036004.

- 506 38. Seok S, Onal CD, Cho K-J, Wood RJ, Rus D, Kim S. Meshworm: A Peristaltic Soft Robot With
507 Antagonistic Nickel Titanium Coil Actuators. *IEEE/ASME Transactions on Mechatronics*.
508 2013;18(5):1485–1497.
- 509 39. Huang X, Kumar K, Jawed MK, Mohammadi Nasab A, Ye Z, Shan W, Majidi C. Highly Dynamic
510 Shape Memory Alloy Actuator for Fast Moving Soft Robots. *Advanced Materials Technologies*.
511 2019;4(4):1800540.
- 512 40. Cruz Ulloa C, Terrile S, Barrientos A. Soft Underwater Robot Actuated by Shape-Memory Alloys
513 “JellyRobcib” for Path Tracking through Fuzzy Visual Control. *Applied Sciences*.
514 2020;10(20):7160.
- 515 41. Umedachi T, Vikas V, Trimmer BA. Softworms : The Design and Control of Non-Pneumatic, 3D-
516 Printed, Deformable Robots. *Bioinspir. Biomim*. 2016;11(2):025001.
- 517 42. Tramsen HT, Gorb SN, Zhang H, Manoonpong P, Dai Z, Heepe L. Inversion of Friction Anisotropy
518 in a Bio-Inspired Asymmetrically Structured Surface. *Journal of The Royal Society Interface*.
519 2018;15(138):20170629.
- 520 43. Sakuma H, Kawai K, Katayama I, Suehara S. What Is the Origin of Macroscopic Friction? *Science*
521 *Advances*. 4(12):eaav2268.

522

523 **Acknowledgments:**

524 **Funding:** L.X. was supported by the National Natural Science Foundation of China
525 (NSFC) with grant 51905222, 51805218, Natural Science Foundation of Jiangsu
526 Province with grant BK20211068, and Senior Talent Scientific Research Fund of
527 Jiangsu University with grant 15JDG179. **Author contributions:** L.X. conceived the
528 idea and concept of the project. S.L. performed the experimental procedures. L.X., S.L.,
529 W.R., D.Z., R.W., and F.V. wrote the manuscript. All authors participated in the data
530 collection, data analysis, and manuscript proof-reading. **Competing interests:** The
531 authors declare that they have no competing interests. **Data and materials availability:**
532 All data needed to evaluate the conclusions in the paper are present in the paper and/or
533 the **Supplementary Materials**. Additional data related to this paper may be requested
534 from the authors.

Supplementary Files

This is a list of supplementary files associated with this preprint. Click to download.

- [S1.mp4](#)
- [S2.mp4](#)
- [S3.mp4](#)
- [S4.mp4](#)
- [S5.mp4](#)
- [S6.mp4](#)
- [S7.mp4](#)
- [S8.mp4](#)
- [S9.mp4](#)
- [S10.mp4](#)
- [S11.mp4](#)
- [S12.mp4](#)
- [MagbotpaperSlv9.pdf](#)
- [S4d1.mp4](#)